Classical and Quantum Gravity

PAPER

Unveiling the cation ratio mediated structural modifications in TiO_2:GeO_2 mixtures for gravitational-wave detectors

To cite this article: Sangita Bhowmick *et al* 2024 *Class. Quantum Grav.* **41** 105007

IOP Publishing Classical and Quantum Gravity
Class. Quantum Grav. **41** (2024) 105007 (13pp) https://doi.org/10.1088/1361-6382/ad3c08

Unveiling the cation ratio mediated structural modifications in TiO_2:GeO_2 mixtures for gravitational-wave detectors

Sangita Bhowmick[1,*], **Ruth Osovsky**[1], **Aaron Davenport**[1], **François Schiettekatte**[2], **Martin Chicoine**[2] **and Carmen S Menoni**[1,*]

[1] Electrical and Computer Engineering, Colorado State University, Fort Collins, CO 80523, United States of America
[2] University of Montreal, Quebec H3T 1J4, Canada

E-mail: sangita1@colostate.edu and Carmen.Menoni@colostate.edu

Received 4 December 2023; revised 29 February 2024
Accepted for publication 8 April 2024
Published 22 April 2024

Abstract

Amorphous thin films of Ti doped GeO_2 are of interest for coatings of the mirrors in gravitational wave detectors (GWDs) due to their low internal friction (Vajente *et al* 2021 *Phys. Rev. Lett.* **127** 071101). The addition of Ti to amorphous GeO_2 (a-GeO_2) enables tailoring of the optical and structural properties of the mixtures. However, the specific modifications that occur in the amorphous network with the addition of Ti are not known. In this work, x-ray photoelectron spectroscopy is used to identify modifications to the bonding of Ge and Ti atoms in mixtures of Ti doped a-GeO_2 with different Ti cation content. The formation of (Ti–O–Ge) bonds is evidenced from: (1) the presence of a peak which intensity increases with Ti content and causes a shift to lower binding energy (BE) of the core level O 1s peak; (2) the shift to higher BE of the Ti $2p_{3/2}$ peak and a decrease in the energy split; and (3) the shift to lower BE of the Ge $3d_{5/2}$ peak and increase in the energy split. These changes reflect modifications to the bonding when Ge replaces Ti in Ti–O–Ti bonds and Ti replaces Ge in Ge–O–Ge bonds due to their difference in electronegativity. A decrease in the O–O nearest-neighbour distance due to the incorporation of Ti atom is also observed from the broadening of the valence band spectra. The results show the 0.44 Ti doped a-GeO_2 mixture has a balance between the (Ti–O–Ge) and the (Ge–O–Ge) networks, not observed in Ti poor and Ti rich mixtures. This

* Authors to whom any correspondence should be addressed.

finding could have important consequences in the optimisation of amorphous Ti doped *a*-GeO_2 mixtures for low internal friction coatings of GWDs.

Supplementary material for this article is available online

Keywords: amorphous oxide thin films, amorphous oxide compounds, TiO_2, GeO_2, x-ray photoelectron spectroscopy

1. Introduction

The mixing of several cations in amorphous oxide compounds makes it possible to controllably modify their electronic, structural, and optical properties [1–4]. This capability has been exploited in many applications, such as in microelectronics [5, 6] and in optics [7, 8]. For optical applications, mixing or doping of a metal cation into an amorphous oxide matrix modifies the refractive index and the extinction at the application wavelength. There are also structural modifications which manifest in increased crystallisation temperature of the matrix, as has been shown in Ta_2O_5 doped with other metal cations [1, 2, 9–11]. The addition of Ti with a cation content of ∼25% into an amorphous oxide matrix of Ta_2O_5 has proven to be essential to lower coating Brownian noise in the multilayer dielectric (MLD) coatings of gravitational wave detectors (GWDs) [9, 12–14]. Coating thermal noise (CTN) arises from elastic energy dissipation predominant in the high index layer of the ∼25% Ti doped Ta_2O_5 [15]. Different studies of doping of Ta_2O_5, both experimental and model simulations, have shown that the addition of Ti or Zr to amorphous Ta_2O_5 alters the atomic network at the medium range which favourably impacts reduction in internal friction [16–18].

The strategy of doping amorphous oxides to increase crystallisation temperature, tailor optical properties and reduce internal friction was also used in an alloy of Ti doped amorphous GeO_2 (*a*-GeO_2), which is a potential alternative candidate to 25% Ti doped Ta_2O_5 as the high index layer material in the MLD coatings of the mirrors of GWD. Experiments showed Ti doped *a*-GeO_2 with 0.44 Ti cation concentration reaches a value of internal friction three times lower than that of 0.25 Ti doped Ta_2O_5 when annealed to 600 °C for 100 h [19]. CTN simulations of MLD coatings of 0.44 Ti doped GeO_2 and SiO_2 with the same design as those of the intermediate and end test masses of advanced Laser Interferometer Gravitational-wave Observatory (LIGO) predict the CTN can reach values 2× lower than that of present coatings [19].

Amorphous GeO_2 (*a*-GeO_2) is a glass former. On the other hand, Ti cations are considered to act as both network formers and network modifiers [20, 21]. Furthermore, the addition of Ti increases its refractive index, which is necessary to tune its optical properties for used in MLD coatings. In analogy to Zr doped Ta_2O_5, one would expect modifications to the network organisation of *a*-GeO_2 with Ti doping [16]. In *a*-GeO_2 the network organisation in the short range consists of tetrahedra formed by the Ge atom connected to bridging oxygen at the corners. These units arrange in rings of different sizes at the medium range [22]. The addition of Ti atoms is expected to alter the network organisation owing to the presence of four-, five- and six-fold coordinated polyhedral units [23, 24]. Therefore, O atoms at each corner, the oxygen bonding environment plays a crucial role in controlling the network organisation at the nearest-neighbour level of amorphous oxide [17]. However, the exact role of Ti in the alteration of the network organisation in Ti doped *a*-GeO_2 (Ti: *a*-GeO_2) has not been studied yet.

Herein, we describe the bonding modifications of *a*-GeO_2 when Ti is incorporated at different cation concentrations. Results of x-ray photoelectron spectroscopy (XPS) from a set of

ion beam sputtered Ti-doped a-GeO_2 with Ti cation concentration between 0 and 0.63 show a systematic evolution of the mixed (Ti–O–Ge) network as compared to pure (Ge–O–Ge) and (Ti–O–Ti) networks as a function of Ti content, demonstrating atomic mixing. Results indicate that Ti doped a-GeO_2 samples with 0.44 Ti cation concentration have a balance between Ti–O–Ge and Ge–O–Ge networks in contrast to Ti-rich and Ti-poor mixtures. Analysis of the near valence band (VB)-XPS spectra of all the as-deposited mixtures shows the variation in orbital's hybridisation upon cation incorporation. The results of this study provide a clear understanding of cation concentration driven atomic structure modification in Ti doped a-GeO_2 which could play a decisive role in reducing mechanical loss.

1.1. Experimental details

Thin films of Ti-doped a-GeO_2 with cation ratio (Ti/Ti + Ge) of 0, 0.10, 0.33, 0.44, 0.63 and 1 were deposited by reactive ion beam sputtering using the Laboratory Alloy and Nanolayer System manufactured by 4Wave, Inc. [19, 25]. In this deposition tool, a low-energy ion source is used to generate a plume of Ar ions which are accelerated towards the metal substrate using a pulsed bias. The desired mixture composition is obtained by sputtering simultaneously the Ti and Ge targets using a bias pulse length that is adjusted to obtain the desired Ti cation content at a selected oxygen partial pressure. The base pressure reached 2×10^{-8} Torr whereas the process pressure was kept near 6×10^{-4} Torr. Deposition parameters for Ti doped a-GeO_2 films with different Ti percentage are given in table S1 of supplementary material (SM).

Ti doped a-GeO_2 thin film mixtures of thickness ranging from 250 to 500 nm were deposited onto silicon substrates for structural characterisation. The dopant cation concentration, atomic areal density, and oxygen stoichiometry of the films were determined through Rutherford backscattering spectrometry (RBS) measurements. These measurements were conducted using He^+ ions with an energy of 2.035 MeV generated by a 1.7 MV Tandetron accelerator. Finally, SIMNRA software was utilised to simulate all RBS spectra [26]. XPS spectra were collected using the Physical Electronics PE 5800 ESCA/ASE spectrometer with monochromatic Al Kα x-rays of energy 1486.6 eV and electron take-off angles of 45°. A charge neutraliser was used with a current of 10 μA for all measurements. The base pressure of the system was around 1×10^{-9} Torr. All the acquired spectra were analysed using CasaXPS software [27]. The electron binding energies (BEs) were then corrected by considering the adventitious carbon C 1s peak at 284.9 eV for all samples which arises due to stray carbon impurities [9]. The results presented herein pertain to the as-deposited thin film mixtures.

1.2. Results and discussion

The evolution of the chemical state of Ti doped a-GeO_2 mixtures with different cation concentration was investigated from the changes in the O 1s, Ti 2p and Ge 3d edges. These peaks in the high resolution XPS spectra were analysed by deconvoluting the oxidation states with a Voigt (70% Gaussian + 30% Lorentzian) function after Shirley background subtraction in CASA XPS. The use of adventitious C 1s peak for the binding energy calibration of the high-resolution spectra introduces an uncertainty of $\pm$0.1 eV in the peak positions [9, 28]. There is also an uncertainty of $\pm$0.1 eV arising from the deconvolution of the peaks with CASA XPS software, resulting in a $\pm$0.2 eV error in peak position.

The high resolution XPS spectra of the O 1s core level for a-GeO_2 and a-TiO_2 are shown in figure 1. As we can see from figure 1(a), the O 1s peak for a-GeO_2 can be deconvoluted into two peaks positioned at 533.3 eV and 532.2 eV (assigned as O1, O2), where the higher intensity peak at 532.2 eV is associated with lattice oxygen, identifying the (Ge–O–Ge) bond

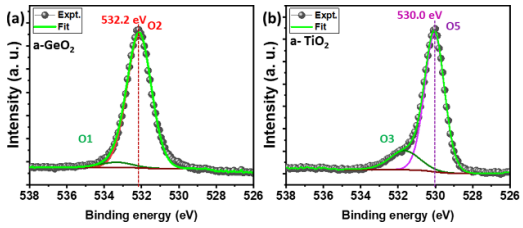

Figure 1. Deconvoluted O 1s XPS spectra for (a) *a*-GeO_2, (b) a-TiO_2.

[29] while the O1 peak is associated to hydroxyl groups attached to Ge atoms (Ge–OH) [30, 31]. For a-TiO_2, the O 1s core level peak (figure 1(b)) also shows the presence of two peaks at 531.6 eV and 530.0 eV (assigned as O3, O5). O3 is associated with –OH molecule attached to Ti (Ti–OH) and O5 is associated with lattice oxygen of a-TiO_2 (Ti–O–Ti) [32–34]. We should note here that the appearance of OH radicals indicate their attachment to surface defects such as oxygen vacancies [34–37].

The O 1s core level in the Ti doped *a*-GeO_2 mixtures shows a complex structure, which is modified as the percentage of Ti in the mixtures increases as shown in figure 2. The shape of the O 1s core level spectrum transforms due to the appearance of a peak at 531.1 eV (assigned as O4 in figure 2). The deconvoluted O 1s peak with O1, O2, O3, O4 and O5 components for Ti doped *a*-GeO_2 are tabulated in the table S2 in supplementary material (SM). Both O1 (Ge–OH) and O3 (Ti–OH) peaks show negligible change with cation concentration. However, as the Ti cation ratio increases the relative intensity of peak O4 increases, as can be seen from figure 2 and table S2 in SM. For the 0.44 cation concentration alloy, the intensity of peak O4 become comparable to the intensity of peak O2. For 0.63 Ti doped *a*-GeO_2 the relative at.% of O5 exceeds O2, due to the increase in Ti–O–Ti contribution as compared to Ge–O–Ge. The fact that the BE value of peak O4 (at 531.1 eV) does not match the BE value of *a*-GeO_2 (at 532.2 eV) or a-TiO_2 (at 530.0 eV) lattice oxygen, indicates O4 is associated with oxygen, which is bonded with both Ti and Ge (i.e. Ti–O–Ge mixed oxide network). Since, the electronegativity of Ti (1.54, using Pauling's scale) is lower than of Ge (2.01, using Pauling's scale), bond weakening in Ge–O–Ge can be significant due to the formation of Ti–O–Ge bonds via incorporation of Ti [38]. These modifications in the bond length shift the overall O1s spectra towards lower BE with increasing Ti content in the mixtures. The evolution of the different O1s components with Ti percentage, as can be seen from figure 2 and table S2, shows a monotonic increase in the relative percentage of O4 (Ti–O–Ge) and a decreasing trend of O2 (Ge–O–Ge) up to 0.44 Ti cation concentration. As depicted in table S2 in SM, the 0.44 Ti-doped *a*-GeO_2 samples exhibit a mixed network of 42% (Ti–O–Ge) and 44% (Ge–O–Ge) bonds. Notably, the relative percentage of the (Ti–O–Ge) network is lower for mixtures with lower cation concentrations (0.10 and 0.33). In 0.63 Ti-doped *a*-GeO_2 while the Ti–O–Ge percentage (41%) is similar to that of the 0.44 Ti-doped *a*-GeO_2, the (Ti–O–Ti) percentage (36%) is high. These results indicate that Ti atoms preferentially form (Ti–O–Ge) bonds rather than Ti–O–Ti bonds up to Ti cation concentrations of 0.44 in contrast to 0.63 Ti doped *a*-GeO_2 in which the Ti–O–Ti network becomes significant.

The changes in the bonding environment of Ti in the Ti doped *a*-GeO_2 mixtures ($0 < \mathrm{Ti} < 1$) were evaluated from the XPS spectra near the Ti 2p level. As shown in figure 3, the Ti 2p peak for a-TiO_2 consists of two main peaks at 458.6 eV and 464.3 eV [39, 40]. The doublet peaks at 458.6 eV (Ti $2p_{3/2}$) and 464.3 eV (Ti $2p_{1/2}$) are associated with Ti^{4+} in the TiO_2 lattice and arise from spin–orbit-splitting between Ti $2p_{3/2}$ and Ti $2p_{1/2}$ (ΔTi 2p $= 5.72 \pm 0.02$ eV). Whereas,

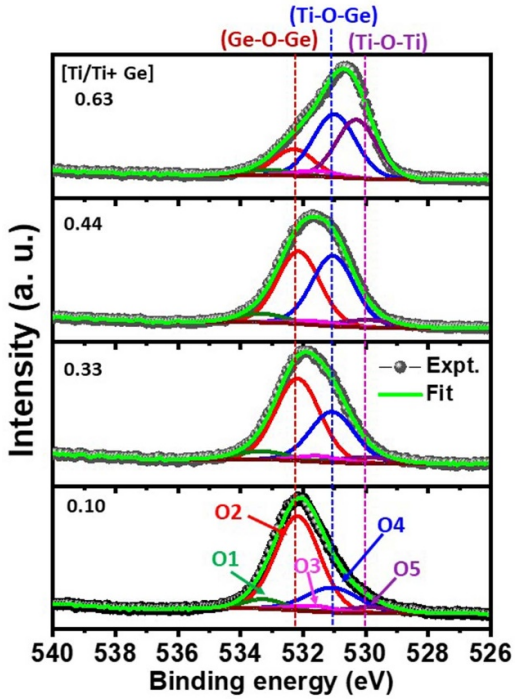

Figure 2. Deconvoluted O 1s core level XPS spectra for as-deposited Ti doped a-GeO_2 mixtures with different Ti cation concentration. The dotted lines indicate the centroids of O2 (Ge–O–Ge), O4 (Ti–O–Ge) and O5 (Ti–O–Ti).

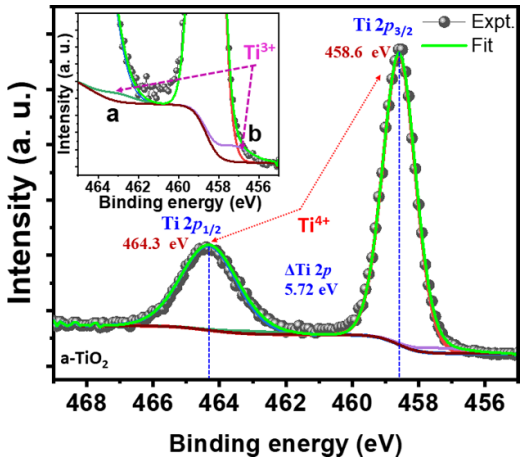

Figure 3. Deconvoluted Ti 2p XPS spectrum for a-TiO_2. The experimental data and fitted curves are shown by black circles and thick green lines, respectively. The Ti 2p XPS is presented in the inset to show the lower BE peaks, associated with Ti^{3+}.

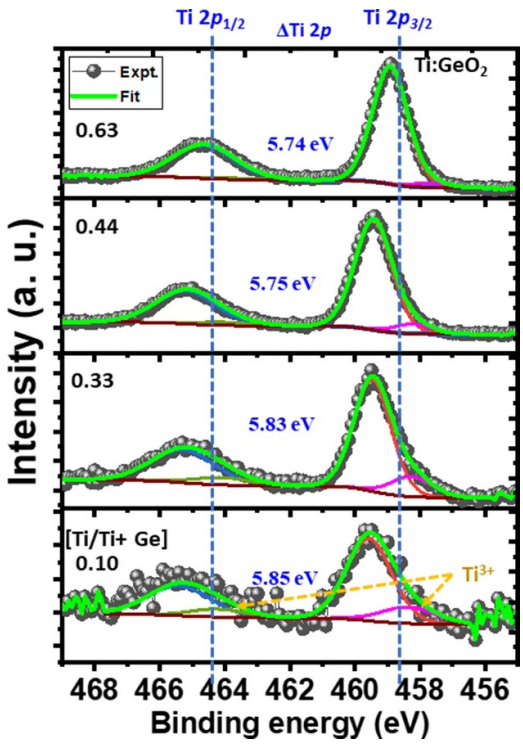

Figure 4. Deconvoluted Ti 2p XPS spectra for all as-deposited Ti doped *a*-GeO_2 mixtures with different Ti cation concentration. Here, blue dotted lines represent the position of Ti $2p_{3/2}$ and Ti $2p_{1/2}$ of a-TiO_2, respectively.

the shoulder peaks at 457.3 eV and 463.0 eV (inset of figure 3) with negligible contribution could be associated with Ti^{3+} in Ti_2O_3 [41, 42].

For all Ti doped *a*-GeO_2 mixtures, the deconvoluted Ti 2p XPS spectra with Ti $2p_{3/2}$ and Ti $2p_{1/2}$ peaks are shown in figure 4. For all the fittings the area ratio for Ti $2p_{3/2}$ and Ti $2p_{1/2}$ was fixed to 2:1. For clarity, the deconvoluted Ti 2p peak positions, their relative intensity (at.%), and the value of ΔTi 2p are tabulated in the table S3 (see SM). As can be seen from figure 4 and table S3 in SM, the Ti 2p peak shifts to higher BE in Ti doped *a*-GeO_2 mixtures as compared to Ti 2p of a-TiO_2. For the mixture with a Ti cation content of 10%, the whole spectrum is shifted by 1 eV to higher BE with respect to a-TiO_2, with the Ti $2p_{3/2}$ at 459.6 eV and Ti $2p_{1/2}$ at 465.4 eV (ΔTi 2p = 5.85 ± 0.02 eV). As the percentage of Ti increases, the Ti 2p peak gradually shifts towards lower BE position. Also, the peak separation for mixtures is significantly different from 5.72 ± 0.02 eV for Ti in a TiO_2 (Ti^{4+}) environment. Such change in the peak separation has previously been attributed to the modifications of the Ti bonding environment and formation of an atomic mixture in Ti doped Ta_2O_5 [9, 25]. The change in the Ti $2p_{3/2}$ peak position and ΔTi 2p of Ti doped *a*-GeO_2 as a function of Ti percentage is represented in figure 5. The results show a clear decreasing trend in the BE of Ti $2p_{3/2}$ along with reduction in the ΔTi 2p value with increasing Ti percentage. This indicates that the chemical environment of the Ti atoms is not same in the mixtures as in a-TiO_2 [9, 43]. As mentioned earlier, Ti has lower electronegativity than Ge. Thus, in the presence of Ge the

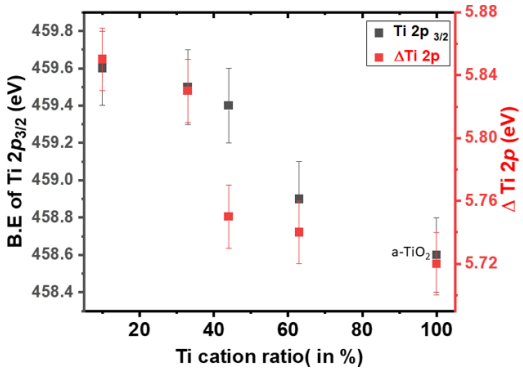

Figure 5. Change in the peak position of Ti $2p_{3/2}$ (black symbols) and ΔTi 2p (red symbols) for Ti doped *a*-GeO_2 versus Ti cation content.

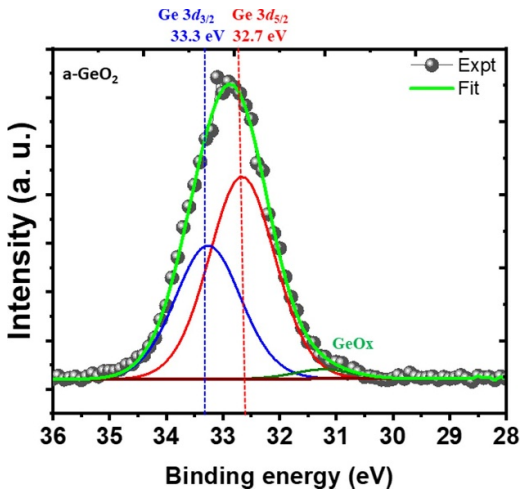

Figure 6. Deconvoluted Ge 3d XPS spectra for *a*-GeO_2. Ge $3d_{3/2}$ and Ge $3d_{5/2}$ components are represented by the blue and red curve, while the small green peak is associated with Ge–OH.

electron density around the Ti decreases and the binding energy increases. Hence, the Ti 2p peak shifts towards lower BE positions as the Ti cation content increases [38]. The observed shift of Ti 2p peak position as well as the change in the value of ΔTi 2p, indicates that the chemical environment of the Ti atoms in Ti doped *a*-GeO_2 mixtures is different than a-TiO_2 probably due to the formation of Ti–O–Ge bonds in the lattice, revealing atomic mixing.

The Ge 3d core level spectrum of *a*-GeO_2 and the spectra of the Ti doped *a*-GeO_2 for different Ti cation content are shown in figures 6 and 7, respectively. The Ge 3d XPS peaks were fitted with a doublet of Voigt functions corresponding to Ge $3d_{3/2}$ and Ge $3d_{5/2}$ components (represented by the blue and red curves in figures 6 and 7, respectively. For all the fittings the area ratio for Ge $3d_{3/2}$ and Ge$3d_{5/2}$ was fixed to 2:3. As can be seen from figure 6, for the *a*-GeO_2, Ge 3d shows two peaks at 33.3 eV and 32.7 eV associated with Ge $3d_{3/2}$ and Ge $3d_{5/2}$

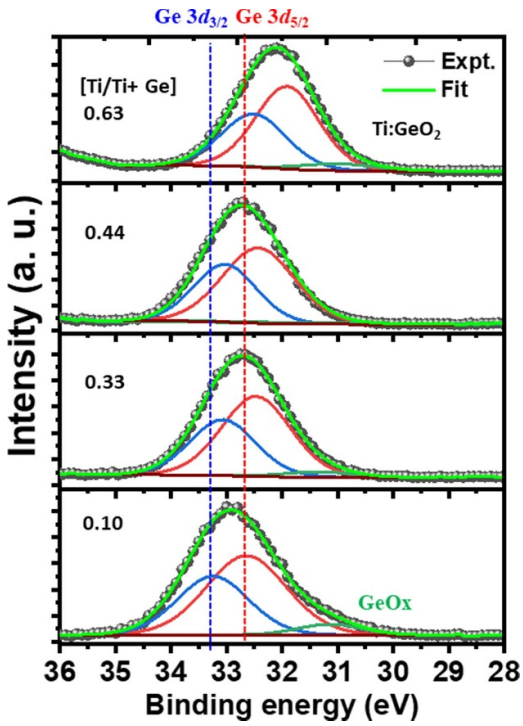

Figure 7. Deconvoluted Ge 3d XPS spectra for all mixed Ti doped *a*-GeO_2 samples. Ge $3d_{3/2}$ and Ge $3d_{5/2}$ components are represented by blue and red curves, while the green curve shows negligible contribution of GeO_x. Here, blue and red dotted lines represent the position of Ge $3d_{3/2}$ and Ge 3d $_{5/2}$ of *a*-GeO_2, respectively.

of GeO_2 (Ge^{4+} oxidation state) with an energy splitting ΔGe 3d $= 0.60 \pm 0.02$ eV. The spin–orbit splitting arises due to the interaction between the electron's spin and its orbital motion. The lower intensity peak at 31.2 eV is associated with GeO_x bonds [29].

As Ti is introduced into the *a*-GeO_2 matrix, the Ge 3d peak position shifts towards lower BE with respect to *a*-GeO_2, as reflected in figure 7. Moreover, the value of spin–orbit splitting (ΔGe 3d) also changes with the incorporation of Ti in the *a*-GeO_2 matrix. For clarity, the deconvoluted Ge 3d peak positions, relative intensity (at.%), and the value of ΔGe 3d are tabulated in table S4 (see SM). The change in the Ge $3d_{5/2}$ peak position and value of ΔGe 3d as a function of Ti percentage are plotted in figure 8. From figure 8 and table S4 in SM, it is clear that BE of Ge $3d_{5/2}$ decreases and ΔGe 3d increases with the increase of Ti content.

For the mixture with 0.44 cation concentration, the energy splitting equals (0.67 ± 0.02 eV). A similar increase in the energy splitting for Ta 4f XPS spectra has previously been reported due to the incorporation of Ti in Ta_2O_5 [9]. The deconvoluted peak positions and relative areas are presented in table S4 (see SM).

Due to the higher electronegativity of Ge (2.01) as compared to Ti (1.54) the electron density on Ge increases upon Ti incorporation. This reduces the binding energy of the electrons attached to Ge. This effect is also evidenced in the energy splitting. Therefore, upon the increase of Ti content, the Ge 3d spectra shifts to lower binding energy and the energy split ΔGe 3d increases compared to the Ge 3d peak of *a*-GeO_2 [38]. These results provide further

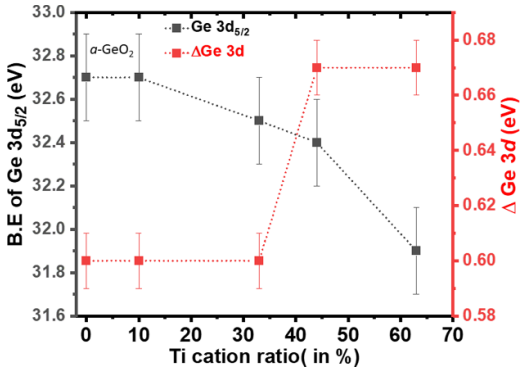

Figure 8. Variations in the peak position of $Ge3d_{5/2}$ (black symbols and left-hand side axis) and value of ΔGe 3d (red symbols and right-hand side axis) for Ti doped a-GeO_2. The dotted lines are for guiding the eye.

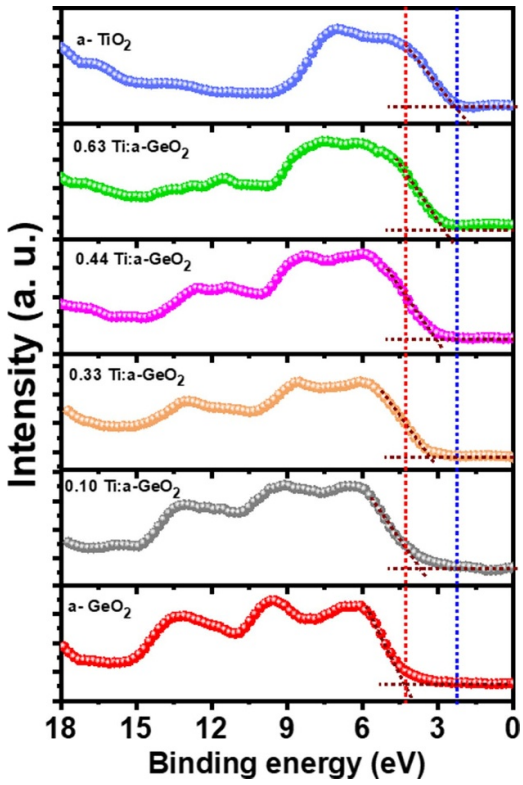

Figure 9. The near valence band VB-XPS spectra for as-grown Ti doped a-GeO_2 samples with different Ti cation content.

support to the strong evidence of charge transfer and formation of a mixed network in Ti doped a-GeO_2 for all Ti contents.

The modifications to the electronic density of states of Ti doped a-GeO_2 mixtures with the incorporation of Ti were obtained from the near VB-XPS spectra of figure 9. A systematic shift to lower BE in the onset of the VB maximum (VBM) position with the increase of Ti content from a-GeO_2 to a-TiO_2 is evident from figure 9.

The position of the VBM is tabulated in table S5 of SM. This shift is expected because the bandgap of a-TiO_2 (Eg $\sim$ 3.4 eV) [44] is smaller than that of a-GeO_2 (Eg $\sim$ 5.6 eV) [45]. Figure 9 also shows the near VBM region in a-GeO_2 contains three peaked structures positioned around $\sim$6.0 eV, $\sim$9.6 eV, and $\sim$13.3 eV. In a-GeO_2, the structure between 4 and 15 eV is derived from the O 2p, Ge 4s, Ge 4p, orbital hybridisation [46, 47]. Instead in a-TiO_2, the near VBM region is composed of two peaked structures positioned around $\sim$4.3 eV, and $\sim$7.0 eV and which arise from the Ti 3d–O 2p orbital hybridisation [46]. It is evident from figure 9 that the shape of the VB spectra in the mixed Ti doped a-GeO_2 changes continuously from a-GeO_2 to a-TiO_2. Since the ionic radius of Ti^{4+} is 68 pm and that of the Ge^{4+} is 54 pm [48], substituting Ti in place of Ge effectively decreases the average O–O separation [46, 49, 50]. It is this separation of the oxygen atoms that is responsible for the broadening of the O 2p nonbonding band and results in the broadening of the VB spectra due to the incorporation of Ti atoms [46, 49]. A similar type of broadening has previously been reported by Fischer et al, in $Si_xGe_{1-x}O_2$ due to the reduction in the average O–O separation [46]. The atomic radius of a Ge atom is larger than that of a Si atom, resulting in the larger bond length of Ge–O = 1.696 Å compared to that of Si–O = 1.606 Å [50]. Therefore, the overall result infers that the Ge–O–Ge bonding configuration transforms into a Ti–O–Ge configuration due to the incorporation of Ti atoms in a-GeO_2 which broadens the VB spectra in the mixtures.

1.3 Conclusions

The analysis of the O 1s, Ti 2p and Ge 3d XPS core level signatures conclusively support the formation of Ti–O–Ge bonds in Ti doped a-GeO_2 mixtures. A systematic increase with Ti content of the (Ti–O–Ge) bonds as compared to (Ge–O–Ge) and (Ti–O–Ti) networks is reflected in the modifications of the O 1s core level in which a peak with BE intermediate between a-GeO_2 and a-TiO_2 appears and grows in intensity. Based on this analysis, the 0.44 Ti-doped a-GeO_2 exhibits a balance in the population of Ti–O–Ge and Ge–O–Ge bonds. The (Ge–O–Ge) network dominates in the 0.10 and 0.33 Ti content mixtures. Instead, the (Ti–O–Ti) network dominates in the 0.63 Ti-doped a-GeO_2 mixture. Further, modifications to the chemical environment of Ti consistent with Ti substituting Ge and vice versa are evident from the shift of the Ti 2p peak to higher binding energy and the shift to lower binding energy of the Ge 3d peak. Additional evidence of atomic mixing is obtained from the decrease in the O–O nearest-neighbour distance due to the incorporation of Ti atom in a-GeO_2 from the broadening of the VB spectra.

The evidence of atomic mixing for all Ti doped a-GeO_2 compounds confirms the simultaneously sputtering of two metal targets in an oxygen rich atmosphere is effective for shaping the structural network organisation in amorphous oxides compounds, as previously shown in Ti doped a-Ta_2O_5 [9]. The substitution of Ge by Ti to form Ti–O–Ge bonds is found in all the mixtures. However, a balance between the Ti–O–Ge and Ge–O–Ge networks is only observed in 0.44 Ti doped a-GeO_2. This specific atomic network organisation has likely played a decisive role in the reduction of mechanical loss of 0.44 Ti doped a-GeO_2, which achieved one of the lowest values reported in amorphous oxide mixtures, $\phi = 0.96 \times 10^{-4}$ after annealing for 108 h at 600 °C [19]. Further insight on the changes in the atomic bonding beyond the results

presented in this paper requires the use of x-ray or electron pair distribution functions [16] or Raman spectroscopy [22] which can identify modifications of the bonding at medium range in Ti doped *a*-GeO_2 alloys that correlate with reduction in mechanical loss.

Data availability statement

All data that support the findings of this study are included within the article (and any supplementary files).

ORCID iDs

Sangita Bhowmick https://orcid.org/0000-0002-4347-4383
François Schiettekatte https://orcid.org/0000-0002-2112-9378

References

[1] Fazio M A, Yang L and Menoni C S 2021 Prediction of crystallized phases of amorphous Ta_2O_5-based mixed oxide thin films using a density functional theory database *APL Mater.* **9** 031106
[2] Choi J, Mao Y and Chang J 2011 Development of hafnium based high-k materials—a review *Mater. Sci. Eng.* R **72** 97–136
[3] Kičas S, Batavičiūtė G, Juškevičius K, Tolenis T, Drazdys R, Buzelis R and Melninkaitis A 2013 Characterization and application of HfO_2-SiO_2 mixtures produced by ion-beam sputtering technology *Proc. SPIE* **8885** 275–81
[4] Acernese F A *et al* 2014 Advanced Virgo: a second-generation interferometric gravitational wave detector *Class. Quantum Grav.* **32** 024001
[5] Kamiya T, Nomura K and Hosono H 2009 Origins of high mobility and low operation voltage of amorphous oxide TFTs: electronic structure, electron transport, defects and doping *J. Disp. Technol.* **5** 273–88
[6] Ho Y-D, Chen K-R, Huang C-L and Kuscer D 2013 Sol–gel-derived amorphous-$MgNb_2O_6$ thin films for transparent microelectronics *J. Am. Ceram. Soc.* **96** 3375–8
[7] Medvedeva J E, Buchholz D B and Chang R P H 2017 Recent advances in understanding the structure and properties of amorphous oxide semiconductors *Adv. Electron. Mater.* **3** 1700082
[8] Becker M, Michel F, Polity A and Klar P 2018 Analysis of the optical parameters of amorphous ternary oxides $Sn_{1-x}Zn_xO$ and $Sn_{1-x}Ni_xO$ processed by combinatorial ion-beam sputter deposition *J. Appl. Phys.* **124** 155701
[9] Fazio M A, Vajente G, Ananyeva A, Markosyan A, Bassiri R, Fejer M M and Menoni C S 2020 Structure and morphology of low mechanical loss TiO_2-doped Ta_2O_5 *Opt. Mater. Express* **10** 1687–703
[10] Fazio M A, Vajente G, Yang L, Ananyeva A and Menoni C S 2022 Comprehensive study of amorphous metal oxide and Ta_2O_5-based mixed oxide coatings for gravitational-wave detectors *Phys. Rev.* D **105** 102008
[11] Zakrzewska K 2001 Mixed oxides as gas sensors *Thin Solid Films* **391** 229–38
[12] Granata M *et al* 2016 Mechanical loss in state-of-the-art amorphous optical coatings *Phys. Rev.* D **93** 012007
[13] Granata M *et al* 2020 Amorphous optical coatings of present gravitational-wave interferometers *Class. Quantum Grav.* **37** 095004
[14] Harry G M *et al* 2006 Titania-doped tantala/silica coatings for gravitational-wave detection *Class. Quantum Grav.* **24** 405
[15] Penn S D *et al* 2003 Mechanical loss in tantala/silica dielectric mirror coatings *Class. Quantum Grav.* **20** 2917
[16] Prasai K *et al* 2019 High precision detection of change in intermediate range order of amorphous zirconia-doped tantala thin films due to annealing *Phys. Rev. Lett.* **123** 045501

[17] Bassiri R, Evans K, Borisenko K, Fejer M, Hough J, MacLaren I, Martin I, Route R and Rowan S 2013 Correlations between the mechanical loss and atomic structure of amorphous TiO_2-doped Ta_2O_5 coatings *Acta Mater.* **61** 1070–7
[18] Jiang J, Li X-G, Mishkin A S, Zhang R, Bassiri R, Fry J N, Fejer M M and Cheng H-P 2023 Amorphous Zirconia-doped tantala modeling and simulations using explicit multi-element spectral neighbor analysis machine learning potentials (EME-SNAP) *Phys. Rev. Mater.* **7** 045602
[19] Vajente G *et al* 2021 Low mechanical loss TiO_2:GeO_2 coatings for reduced thermal noise in gravitational wave interferometers *Phys. Rev. Lett.* **127** 071101
[20] Farges F, Brown G E Jr, Navrotsky A, Gan H and Rehr J R 1996 Coordination chemistry of Ti (IV) in silicate glasses and melts: III. Glasses and melts from ambient to high temperatures *Geochim. Cosmochim. Acta* **60** 3055–65
[21] Chandrasekhar H, Chandrasekhar M and Manghnani M H 1980 Phonons in TiO_2 SiO_2 glasses *J. Non-Cryst. Solids* **40** 567–75
[22] Yang L *et al* 2021 Enhanced medium-range order in vapor-deposited germania glasses at elevated temperatures *Sci. Adv.* **7** eabh1117
[23] Farges F, Brown G E Jr, Navrotsky A, Gan H and Rehr J J 1996 Coordination chemistry of Ti (IV) in silicate glasses and melts: II. Glasses at ambient temperature and pressure *Geochim. Cosmochim. Acta* **60** 3039–53
[24] Henderson G S and Fleet M E 1995 The structure of Ti silicate glasses by micro-Raman spectroscopy *Can. Mineral.* **33** 399–408
[25] Yang L, Fazio M, Vajente G, Ananyeva A, Billingsley G, Markosyan A, Bassiri R, Fejer M M and Menoni C S 2020 Structural evolution that affects the room-temperature internal friction of binary oxide nanolaminates: implications for ultrastable optical cavities *ACS Appl. Nano Mater.* **3** 12308–13
[26] Mayer M 1999 SIMNRA, a simulation program for the analysis of NRA, RBS and ERDA *AIP Conf. Proc.* **475** 541–4
[27] Fairley N *et al* 2021 Systematic and collaborative approach to problem solving using x-ray photoelectron spectroscopy *Appl. Surf. Sci. Adv.* **5** 100112
[28] Biesinger M C, Payne B P, Lau L W M, Gerson A and Smart R S C 2009 X-ray photoelectron spectroscopic chemical state quantification of mixed nickel metal, oxide and hydroxide systems *Surf. Interface Anal.* **41** 324–32
[29] Molle A, Spiga S and Fanciulli M 2008 Stability and interface quality of GeO_2 films grown on Ge by atomic oxygen assisted deposition *J. Chem. Phys.* **129** 011104
[30] Matsumoto T, Ishikawa S, Saito M, Ueda W and Motohashi T 2022 Studies on activation factors for oxidative coupling of methane over lithium-based silicate/germanate catalysts *Catal. Sci. Technol.* **12** 75–83
[31] Mura A, Hideshima I, Liu Z, Hosoi T, Watanabe H and Arima K 2013 Water growth on GeO_2/Ge (100) stack and its effect on the electronic properties of GeO_2 *J. Phys. Chem.* C **117** 165–71
[32] Fan C, Chen C, Wang J, Fu X, Ren Z, Qian G and Wang Z 2015 Black hydroxylated titanium dioxide prepared via ultrasonication with enhanced photocatalytic activity *Sci. Rep.* **5** 11712
[33] Wiatrowski A, Mazur M, Obstarczyk A, Wojcieszak D, Kaczmarek D, Morgiel J and Gibson D 2018 Comparison of the physicochemical properties of TiO_2 thin films obtained by magnetron sputtering with continuous and pulsed gas flow *Coatings* **8** 412
[34] Das D, Barman A, Kumar S, Sinha A, Gupta M, Singhal R, Johari P and Kanjilal A 2019 Synergistic effect of singly charged oxygen vacancies and ligand field for regulating transport properties of resistive switching memories *J. Phys. Chem.* C **123** 26812–22
[35] Yan J, Wu G, Guan N, Li L, Li Z and Cao X 2013 Understanding the effect of surface/bulk defects on the photocatalytic activity of TiO_2: anatase versus rutile *Phys. Chem. Chem. Phys.* **15** 10978–88
[36] Saini C, Barman A, Das D, Satpati B, Bhattacharyya S, Kanjilal D, Ponomaryov A, Zvyagin S and Kanjilal A 2017 Role of oxygen vacancy on the hydrophobic behavior of TiO_2 nanorods on chemically etched Si pyramids *J. Phys. Chem.* C **121** 278–83
[37] Zheng Z, Teo J, Chen X, Liu H, Yuan Y, Waclawik E R, Zhong Z and Zhu H 2010 Correlation of the catalytic activity for oxidation taking place on various TiO_2 surfaces with surface OH groups and surface oxygen vacancies *Chemistry* **16** 1202–11
[38] Mitrovic I *et al* 2014 Ge interface engineering using ultra-thin La_2O_3 and Y_2O_3 films: a study into the effect of deposition temperature *J. Appl. Phys.* **115** 114102
[39] Bharti B, Kumar S, Lee H-N and Kumar R 2016 Formation of oxygen vacancies and Ti^{3+} state in TiO_2 thin film and enhanced optical properties by air plasma treatment *Sci. Rep.* **6** 32355

[40] Lee T-Y, Lee C-Y and Chiu H-T 2018 Enhanced photocatalysis from truncated octahedral bipyramids of anatase TiO_2 with exposed {001}/{101} facets *ACS Omega* **3** 10225–32
[41] Saari J *et al* 2022 Tunable Ti^{3+}-mediated charge carrier dynamics of atomic layer deposition-grown amorphous TiO_2 *J. Phys. Chem.* C **126** 4542–54
[42] Feng N, Liu F, Huang M, Zheng A, Wang Q, Chen T, Cao G, Xu J, Fan J and Deng F 2016 Unravelling the efficient photocatalytic activity of boron-induced Ti^{3+} species in the surface layer of TiO_2 *Sci. Rep.* **6** 34765
[43] Filatova E, Konashuk A, Sakhonenkov S, Sokolov A and Afanas'ev V 2017 Re-distribution of oxygen at the interface between γ-Al_2O_3 and TiN *Sci. Rep.* **7** 4541
[44] Astinchap B and Laelabadi K G 2019 Effects of substrate temperature and precursor amount on optical properties and microstructure of CVD deposited amorphous TiO_2 thin films *J. Phys. Chem. Solids* **129** 217–26
[45] Liu K, Hwang C S and Choi J-H 2019 A first-principles study on the oxygen adsorption and interface characteristics with a-GeO_2 of Ge[001] nanowire *J. Korean Phys. Soc.* **75** 283–7
[46] Fischer B, Pollak R, DiStefano T and Grobman W 1977 Electronic structure of SiO_2, $Si_xGe_{1-x}O_2$, and GeO_2 from photoemission spectroscopy *Phys. Rev.* B **15** 3193
[47] Shaposhnikov A, Perevalov T, Gritsenko V, Cheng C H and Chin A 2012 Mechanism of GeO_2 resistive switching based on the multi-phonon assisted tunneling between traps *Appl. Phys. Lett.* **100** 243506
[48] Han Z, Yu Y and Cao Y 2018 Doping mechanism of Ge^{4+} ions in Ge^{4+}-doped TiO_2 *Phys. Status Solidi* b **255** 1700289
[49] Rino J-P and Studart N 1999 Structural correlations in titanium dioxide *Phys. Rev.* B **59** 6643
[50] Tamura T, Lu G-H, Yamamoto R and Kohyama M 2004 First-principles study of neutral oxygen vacancies in amorphous silica and germania *Phys. Rev.* B **69** 195204